Supporting Information

A computational framework for tuning intra- and intermolecular ductility in polyurethanes

Chenxi Sheng[1,2,†], Meng Huang[1,†], Andrew P. Dove[2,*], & Linjiang Chen[1,2,*]

[1] State Key Laboratory of Precision and Intelligent Chemistry, University of Science and Technology of China, Hefei, China
[2] School of Chemistry, University of Birmingham, Birmingham, UK

† These authors contributed equally: C.S. & M.H.
* Corresponding authors: a.dove@bham.ac.uk (A.P.D.) & linjiangchen@ustc.edu.cn (L.C.)

Table of Contents

External Force Explicitly Included (EFEI) formalism

In 2009, Marx et. al. introduced the External Force is Explicitly Included (EFEI) method, providing a robust framework for calculating the molecular geometry structure under constant external mechanical stress within computational simulations.[1, 2] This method requires the definition of two specific atoms as the force site describing the vector of external force, while a constant magnitude, F_{ext}, represents the force intensity.[1, 2] Then the method modifies the potential energy surface (PES) by accounting for the mechanical work performed on the system, it tilted by an external force and is given by Eq. 1.

$$V_{EFEI}(\vec{x}, \vec{F}_{ext}) = V_{BO}(\vec{x}) - \vec{F}_{ext} r(\vec{x}) \qquad (1)$$

where, $V_{BO}(\vec{x})$ is the Born-Oppenheimer PES, and $\vec{x}$ is the positional coordinate of the molecule system. For it only shows the vector of the external force, it can be used to test both the bonded and non-bonded force.

Reactive force-field (ReaxFF) details

Reactive Force-Field Method (ReaxFF) is a relevant force field method which can describe the formation and breakage of bonds.[3] It was invented in 2001 by van Duin et. al. to simulate a 1000-atom system and calculate the formation heat when some hydrocarbons burn.[4] This method is a general bond-order-dependent potential including van der Waals and Coulomb force, and it is kept the central force formalism. The total potential energy is given by Eq. 2:

$$E_{total} = E_{bond} + E_{over} + E_{under} + E_{val} + E_{pen} + E_{tors} + E_{conj} + E_{vdWaals} + E_{Coulomb}$$

where, E_{bond} is the bond energy. E_{over} and E_{under} are the overcoordination and undercoordination energy, which is for periodical system. E_{val} is valence angle energy. E_{pen} is the penalty energy. E_{tors} is the dihedral energy. E_{conj} is the conjugation energy. $E_{vdWaals}$ is van der Waals interactions. And $E_{Coulomb}$ is Coulomb energy about electrostatic interaction. Apart from the latter two, all others are bonded energy. The other two are non-bonded energy.[5]

Classical MD simulations of double chains

Classical MD simulations of the double PU chains studied by EFEI were conducted using the LAMMPS package.[13, 14] Atomistic force-field parameters were generated with the LigParGen web server, which provides OPLS-AA/CM1A-LBCC parameters suitable for organic systems.[13-17]

Each system was placed in a 100 × 100 × 100 Å³ simulation box with periodic boundary conditions. An initial NVT simulation at 500 K was run for 8 ns with a time step of 0.001 ps, using a Langevin thermostat for temperature control. During the production phase, configurations were saved every 2 ps over the last 4 ns, yielding 2000 configurations per system.

Hydrogen bonds were identified geometrically: a hydrogen bond was counted when the hydrogen–acceptor distance was < 2.0 Å and the donor–hydrogen–acceptor angle exceeded 135°.[18] These criteria were used to compute ensemble-averaged hydrogen-bond statistics for each combination of dynamic bond and hydrogen-bonding moieties under higher temperature of 500 K.

Benchmark study of EFEI method for intramolecular and intermolecular ductility

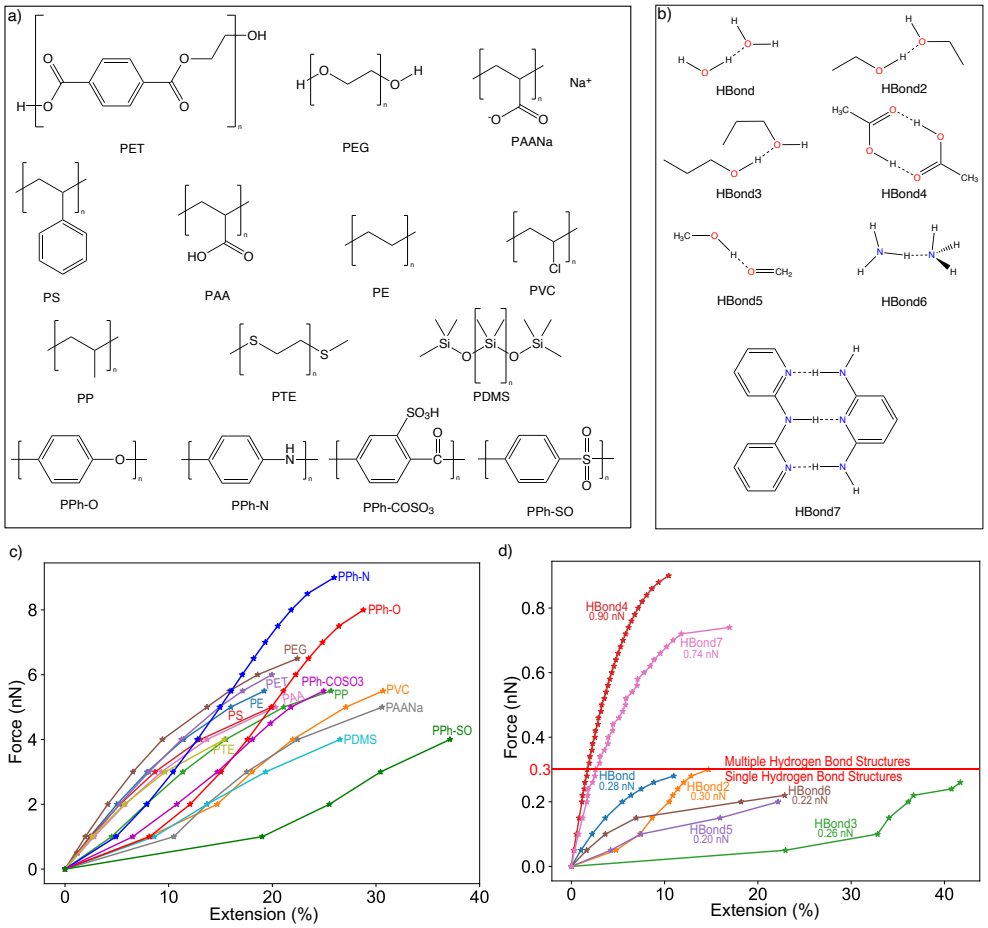

Figure S1. Benchmark polymer structures and stress–strain responses used to validate the workflow. (a) Chemical structures of fourteen representative "standard" polymers together with corresponding stress–strain curves. (b) Schematic definitions of the seven molecular systems that include hydrogen-bonding interactions. (c) Stress–strain curves of twelve typical polymers[19-21] (d) Stress–strain curves of seven hydrogen-bonded polymer systems.

All density functional theory (DFT) calculations were performed with ORCA 5.0.[6] For the benchmark polymer set, we used B3LYP/def2-TZVP[7, 8] with Grimme's D3(BJ) dispersion correction.[9, 10] Calculations employed the grid4 integration grid. Constant external forces were applied using the EFEI implementation in ORCA,[11] with force-application sites placed at the two ends of the relevant polymer segment.[12]

Because EFEI has rarely been used to define polymer scission points at the DFT level, we performed benchmark calculations to validate the approach. Scission points were identified from force–distance curves that describe the mechanical response of representative monomers under increasing external force.

Force–extension profiles for 14 representative linear repeat units are shown in Figure S1a. The x-axis denotes the symmetric extension applied to both ends of the monomer, and the y-axis reports the applied force. As the external force increases, the monomer elongates, producing an initial rising region in the

force–distance curve. The termination of the curve marks the scission point (Fmax), i.e., the critical force at which covalent bond cleavage occurs and the monomer loses structural integrity.

The initial straightening step varies across the different monomers because their force-free geometries are not necessarily linear. Monomers that adopt coiled conformations stabilized by noncovalent interactions (e.g., hydrogen bonding, halogen bonding, or π–π stacking) can show an unusually shallow initial slope, reflecting progressive straightening before backbone stretching dominates.

Figure S1c summarizes the scission forces for the benchmark set. Most representative monomers rupture within ~5.0–6.0 nN. For nonconjugated backbones, incorporation of smaller heteroatoms (O or N) tends to increase the scission force; for example, PEG sustains ~6.5 nN, whereas PE ruptures at ~5.5 nN. This trend is consistent with shorter, stronger C–O bonds in PEG (~1.42 Å) relative to C–C bonds in PE (~1.53 Å).[22] In contrast, backbones containing heavier third-row elements are more fragile: polythioethylene (PTE) and PDMS rupture at ~4.0 nN, consistent with longer C–S (~1.82 Å) and Si–O (~1.63 Å) bonds.[22]

Introducing nonconjugated (or weakly conjugated) side groups has only a minor effect on the scission force. For example, PVC shows a scission force (~5.5 nN) similar to PE, as chlorine substitution changes the relevant bond dissociation energies only slightly (~2 kJ·mol−1). Likewise, methyl branching in PP introduces hyperconjugation that weakens adjacent C–C bonds only modestly (also ~2 kJ·mol−1),[23, 24] leading to a scission force comparable to PE.[22]

For conjugated systems, the impact of conjugation depends strongly on its position relative to the backbone. When a conjugated group resides on a side chain (e.g., PS and PAA), the scission force decreases (to ~5.0 nN) relative to PE because the conjugated group can stabilize radical intermediates formed upon bond cleavage.[23, 25] Correspondingly, the C–C bond connecting the conjugated substituent to the backbone has a reduced dissociation energy (≈40 kJ·mol−1 lower than ethane),[22] and scission produces an expanded conjugated fragment that is thermodynamically stabilized.

Conversely, when conjugation is incorporated into the backbone, it can enhance mechanical stability. For example, PET sustains ~6.0 nN, as phenylene units increase the stability of adjacent backbone bonds.[23, 25] This reinforcement is partly offset by ester linkages, which act as electronically weaker sites; accordingly, the net increase relative to PE is modest. In our calculations, PET scission occurs at the ester moiety, yielding CO2 and radical fragments (Figure S2a).

To further probe conjugation effects, we examined four aromatic-backbone architectures in which phenylene rings alternate with amine, ether, carbonyl, or sulfone units (Figure S1c). Systems containing O or N adjacent to the aromatic ring show particularly high scission forces (>8.0 nN), consistent with resonance donation that extends conjugation and strengthens the backbone. In PPh-COSO3, the sulfonyl substituent has little influence on backbone scission, and the system remains relatively stable (~6.0 nN) even though carbonyl cleavage can generate CO fragments. By contrast, incorporation of a sulfone linkage in PPh-SO significantly weakens the backbone (scission at ~4.0 nN), and the sulfone moiety tends to fragment into SO2 under force. Overall, these benchmarks illustrate that aromatic units can reinforce polymer backbones, while functional groups such as sulfones, carbonyls, and esters may act as mechanical weak links.

Finally, converting a functional group to its salt form has little effect on the scission force of the backbone in this benchmark. For example, PAANa (deprotonated PAA) shows a scission force similar to PAA (~5.0 nN).

In summary, these benchmark calculations suggest several practical principles for estimating scission forces. The scission point is governed by the weakest covalent bond along the pulling direction. Mechanical stability generally increases with shorter bond lengths in the backbone. Conjugation is highly regioselective: backbone conjugation tends to strengthen a polymer chain, whereas side-chain conjugation can weaken adjacent backbone bonds by stabilizing radical products. Finally, functional groups such as sulfones, carbonyls, and esters can act as mechanical bottlenecks, even in otherwise reinforced (aromatic) systems.

In addition to covalent scission, we benchmarked EFEI for noncovalent separation by applying external forces to hydrogen-bonded molecular pairs, which serve as simplified models for intermolecular interactions relevant to polymer cohesion.

Force–distance curves for seven hydrogen-bonded systems are shown in Figure S1b. HBond1 corresponds to a water dimer, HBond2 to an ethanol dimer, and HBond3 to the O–H···O interaction in propanol. HBond4 represents a carboxylic-acid dimer (two hydrogen bonds), HBond5 an alcohol···carbonyl interaction, HBond6 an ammonia dimer, and HBond7 a heterocycle N···H–N interaction.

Figure S1d shows that EFEI captures hydrogen-bond rupture at forces far below covalent bond scission. While a typical C–C bond has a dissociation energy on the order of ~80 kcal·mol−1, hydrogen bonds are typically ~7 kcal·mol−1.[26-28] Consistently, PE backbone scission occurs at ~5.5 nN, whereas individual hydrogen bonds rupture at ~0.3 nN. The large separation in force scales supports the sensitivity of EFEI across distinct interaction strengths.

HBond1–3 (water, ethanol, propanol) rupture at similar forces (~0.30 nN), consistent with comparable hydrogen-bond acceptor strengths (as reflected by proton-sharing basicity values β for methanol (0.82) and water (0.64)).[29] HBond6 (ammonia) ruptures at ~0.22 nN, and HBond5 (alcohol···carbonyl) at ~0.20 nN, consistent with their weaker hydrogen-bond energies.[30] In contrast, HBond4 (carboxylic-acid dimer) and HBond7 (heterocycle pair) rupture at substantially higher forces (0.90 and 0.74 nN, respectively), reflecting the stabilizing effect of multiple hydrogen bonds and/or structural complementarity.[29] A characteristic signature of hydrogen-bond rupture, similar to covalent cleavage, is an abrupt geometric transition: prior to rupture, the donor–acceptor separation changes little; at the rupture point it increases sharply, signaling loss of the intermolecular interaction.

Overall, these benchmarks confirm that EFEI can reliably capture the rupture of hydrogen bonds and that the number (and cooperativity) of hydrogen bonds within a molecular pair is a major determinant of the separation force.

Together, the covalent-bond and hydrogen-bond benchmarks indicate that EFEI provides a reliable tool to estimate scission forces for both bonded and non-bonded interactions, supporting its use in the systematic evaluation of mechanochemical responses in the PU systems studied here.

Fragments after the scission of single chains

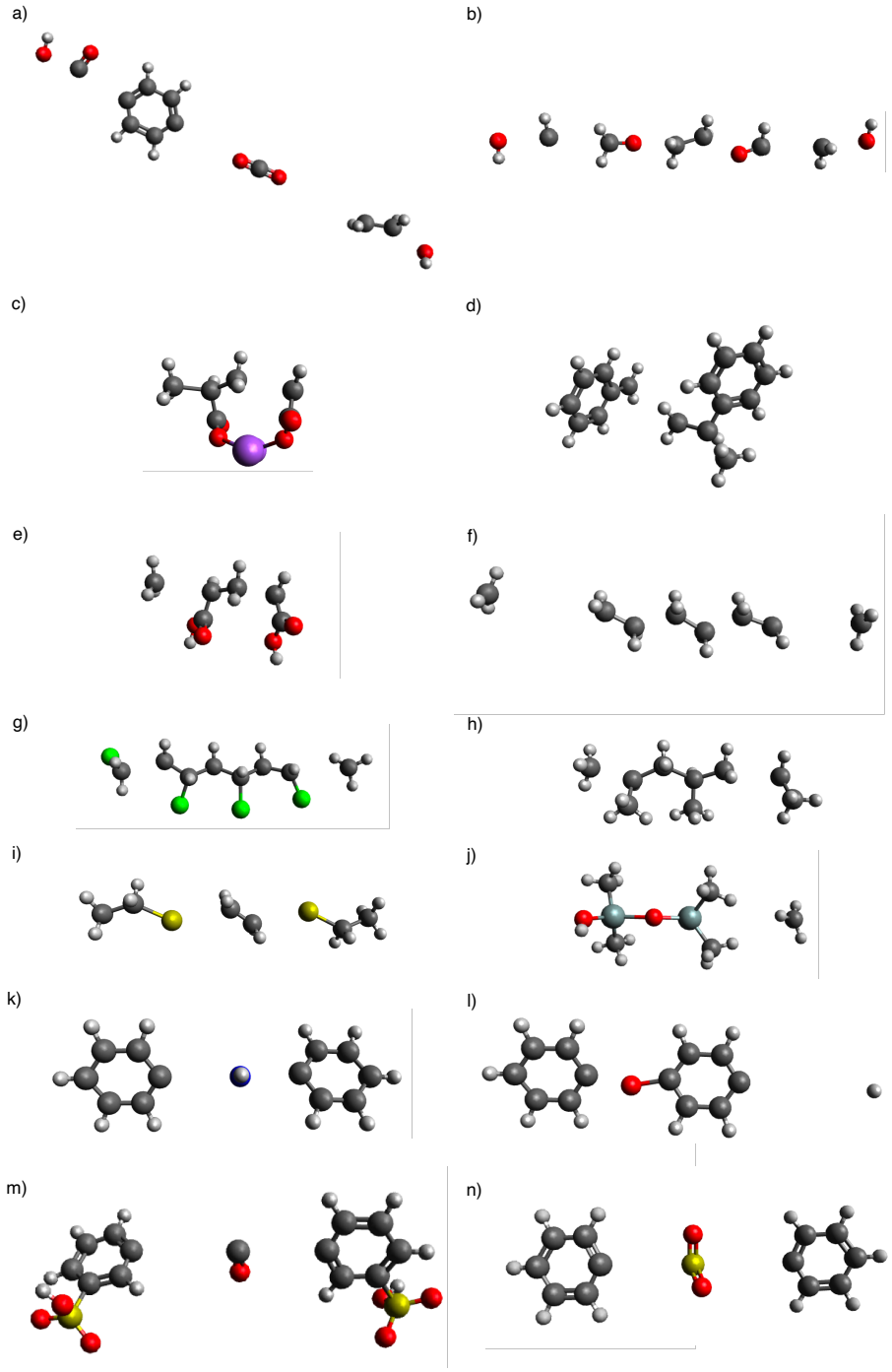

Figure S2. Representative fragments generated after scission in the benchmark set. (a) PET fragments, including phenylene-containing species and CO2; (b) PEG fragments; (c) PAANa fragments, featuring conjugated carboxylate groups with Na+ interactions; (d) PS fragments (phenyl-containing); (e) PAA fragments, featuring conjugated carboxylic-acid groups; (f) PE fragments; (g) PVC fragments; (h) PP fragments; (i) PTE fragments showing C–S bond cleavage; (j) PDMS fragments; (k) PPh–N fragments; (l) PPh–O fragments; (m) PPh–COSO3 fragments, including CO; and (n) PPh–SO fragments, including SO2.

Fragments after the scission of polyurethanes (PU) single chains

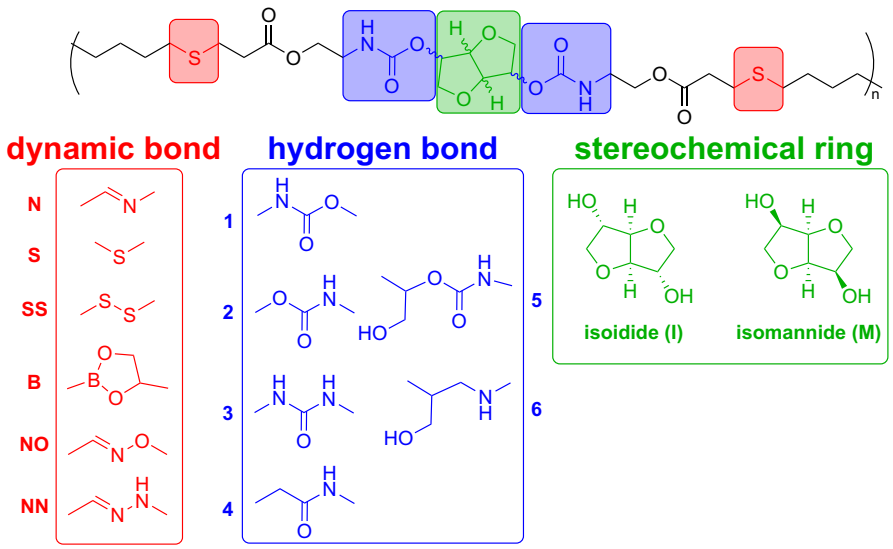

Figure S3. Modular design space of isohexide-based polyurethanes. The PU repeat unit is parameterized by three motif classes: (i) dynamic-bond moieties (red) incorporated in the polymer backbone; (ii) hydrogen-bonding moieties (blue) with varying numbers and spatial arrangements of hydrogen-bond donors and acceptors; and (iii) stereochemical rings (green), either isoidide (I) or isomannide (M), that define the backbone stereochemistry. These modular combinations generate the library of PU structures investigated in this study.

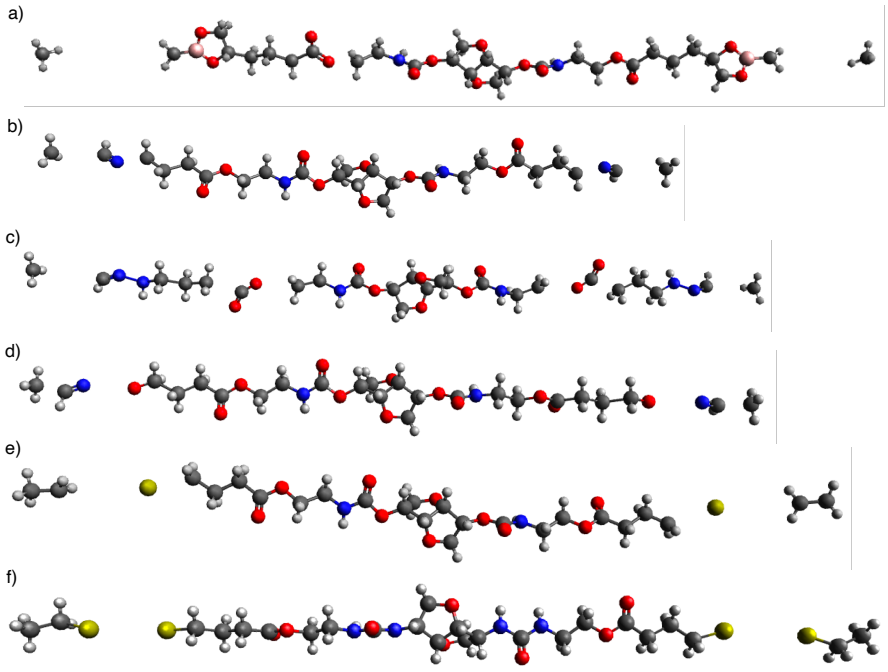

Figure S4. The fragment after the scission of IIPU with original hydrogen-bonding moiety and with dynamic-bond a) moiety B, (b) moiety N and (c) moiety NN, (d) moiety NO, e) moiety S and f) moiety SS.

The scission fragments are determined by the weakest bond along the pulling direction. As shown in Figure S4, most modified IIPU chains rupture within the dynamic-bond moiety. For S and SS, cleavage occurs at the C–S bond. For N and NO, scission occurs at the bond adjacent to the nitrogen-containing conjugated unit, consistent with weakening of bonds next to a conjugated system. The C–C bond connecting the dynamic-bond moiety is also a common cleavage site. Two notable exceptions are observed: (i) for NN, the dynamic bond is sufficiently robust that the hydrogen-bonding moiety ruptures first, followed by the dynamic bond; and (ii) for the boron-ring motif, B–containing bonds resist scission such that cleavage shifts to the adjacent C–C bond (consistent with the strong Lewis acidity of boron).

Distributions of hydrogen-bond numbers across hydrogen-bonding moieties

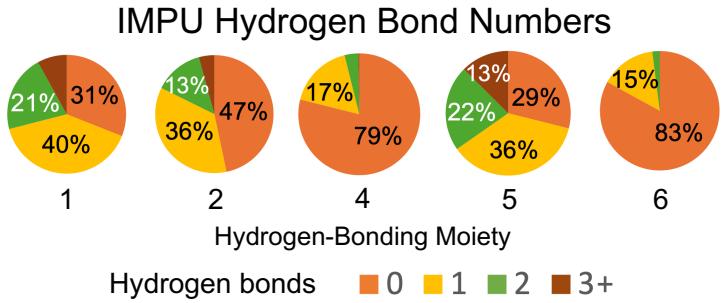

Figure S5. Hydrogen-bond number distributions for IMPU chain-pair simulations. Distributions of hydrogen-bond counts obtained from MD trajectories for IMPU double-chain systems containing hydrogen-bonding moieties 1, 2, 4, 5, and 6 with an N-type dynamic-bond moiety. Colours indicate the fraction of configurations containing 0, 1, 2, or ≥3 hydrogen bonds.

To compare different hydrogen-bonding motifs, we performed MD simulations of IMPU double-chain systems for hydrogen-bonding moieties 1, 2, 4, 5, and 6 using an N-type dynamic-bond moiety (Figure S5). Moiety 5 shows the highest fraction of hydrogen-bonded configurations (~71%) and is the only case in which >10% of configurations contain three or more hydrogen bonds. Moiety 1 most commonly forms a single hydrogen bond (~40%), with ~21% of configurations forming two hydrogen bonds. In contrast, moiety 2 has a higher fraction of configurations with no hydrogen bonds (~47%), with 36% forming one hydrogen bond and 13% forming two. For moieties 4 and 6, hydrogen bonding is strongly suppressed: ~80% of configurations contain no hydrogen bonds and only ~15% contain one.

These results indicate that the number and accessibility of hydrogen-bonding sites strongly influence hydrogen-bond populations. Moiety 5, which can form up to four hydrogen bonds, yields the largest fraction of hydrogen-bonded configurations, whereas moieties 4 and 6 (two sites) show substantially fewer hydrogen-bonded configurations. Moieties 1 and 2 (three sites) display intermediate behavior; the lower hydrogen-bonding frequency for moiety 2 may arise because its amide N–H donor is closer to the stereochemical ring, where ring oxygen atoms can compete as acceptors.

Hydrogen-bond trajectories for selected IMPU double-chain simulations

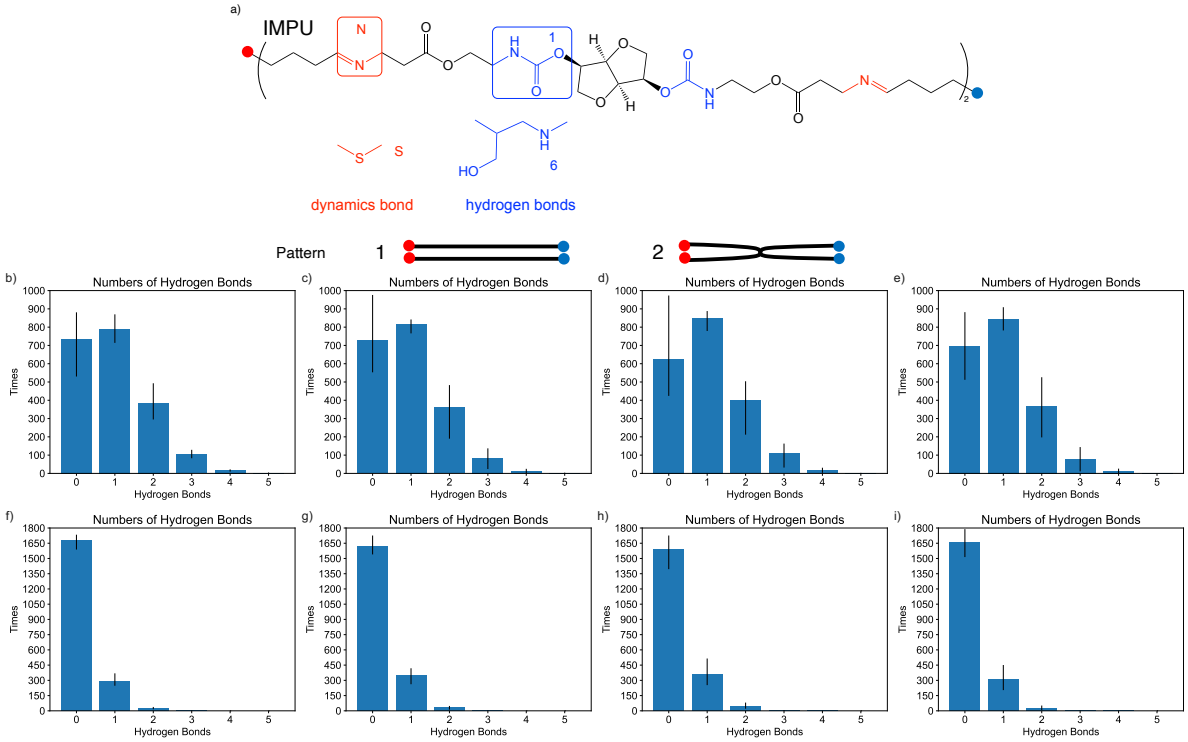

Figure S6. Effect of initial chain-pair geometry on hydrogen-bond statistics in IMPU simulations. (a) Two initial configurations for IMPU chain pairs: Pattern 1, two straight chains without crossover; and Pattern 2, two chains with a single crossover. (b–e) Distributions of the number of hydrogen bonds sampled along MD trajectories for IMPU systems containing hydrogen-bonding moiety 1 with N-type (b,c) or S-type (d,e) dynamic-bond moieties in Pattern 1 (b,d) and Pattern 2 (c,e). (f–i) Corresponding hydrogen-bond number distributions for IMPU systems containing hydrogen-bonding moiety 6 with N-type (f,g) or S-type (h,i) dynamic-bond moieties in Pattern 1 (f,h) and Pattern 2 (g,i).

Hydrogen-bond trajectories for selected IIPU double-chain simulations

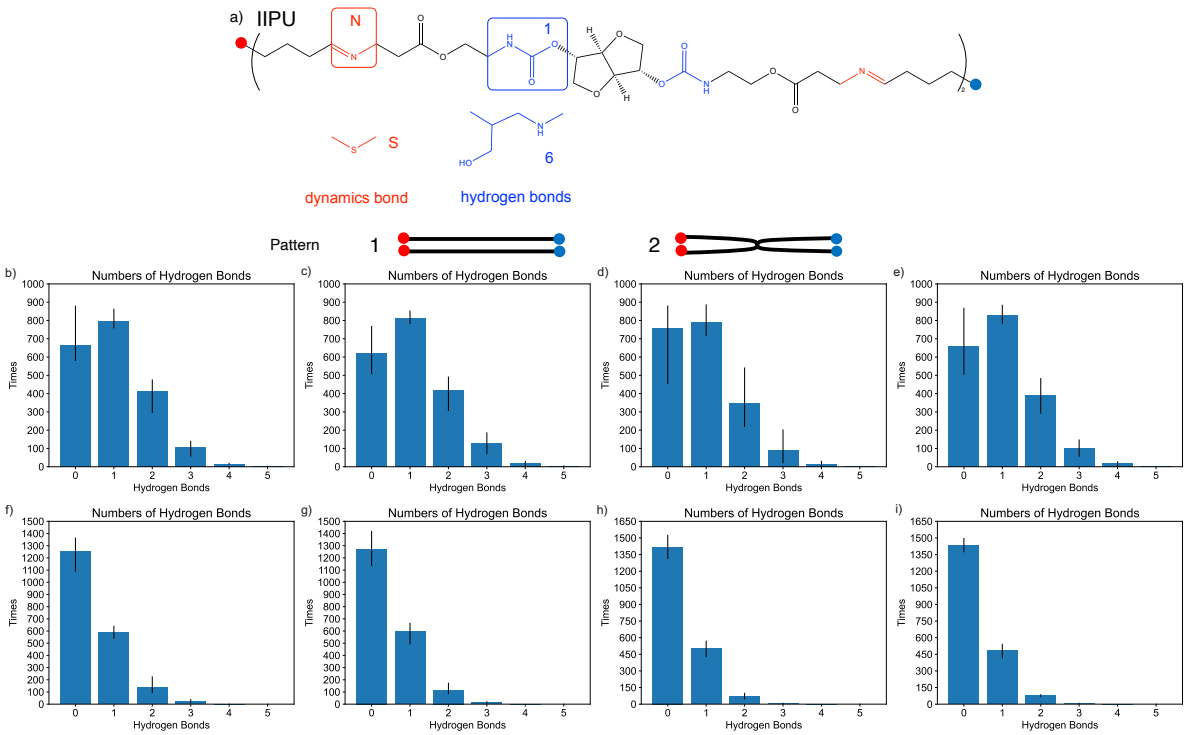

Figure S7. Effect of initial chain-pair geometry on hydrogen-bond statistics in IIPU simulations. (a) Two initial configurations for IIPU chain pairs: Pattern 1, two straight chains without crossover; and Pattern 2, two chains with a single crossover. (b–e) Distributions of the number of hydrogen bonds sampled along MD trajectories for IIPU systems containing hydrogen-bonding moiety 1 with N-type (b,c) or S-type (d,e) dynamic-bond moieties in Pattern 1 (b,d) and Pattern 2 (c,e). (f–i) Corresponding hydrogen-bond number distributions for IIPU systems containing hydrogen-bonding moiety 6 with N-type (f,g) or S-type (h,i) dynamic-bond moieties in Pattern 1 (f,h) and Pattern 2 (g,i).

Hydrogen-bond geometry statistics in IMPU polymer structures

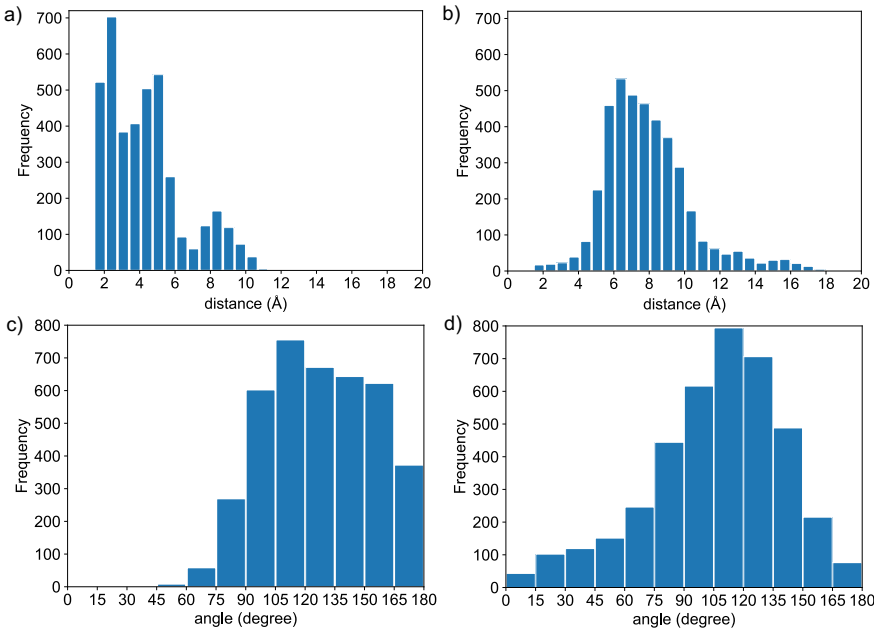

Figure S8. Hydrogen-bond geometry fluctuations in representative IMPU chain-pair systems. Temporal evolution of hydrogen-bond geometries during MD simulations of the N1M (hydrogen-bonding moiety 1) and N6M (hydrogen-bonding moiety 6) chain-pair systems: (a) H···A (hydrogen–acceptor) distance for N1M; (b) H···A distance for N6M; (c) donor–H···acceptor angle for N1M; and (d) donor–H···acceptor angle for N6M. The horizontal cutoffs indicate the geometric criteria used to identify hydrogen bonds (H···A < 2.0 Å; donor–H···acceptor angle > 135°).

The hydrogen-bond geometries in moiety 1 are substantially more stable than those in moiety 6. As shown in Figure S8a and S8c, the N1M system maintains >500 configurations with H···A distances shorter than 2.0 Å and ~1600 configurations with donor–H···acceptor angles exceeding 135°. In contrast, N6M exhibits markedly fewer configurations satisfying these criteria (Figure S8b and S8d): fewer than 30 frames show H···A < 2.0 Å, and only ~750 frames maintain angles >135°. These results indicate that moiety 6 not only forms hydrogen bonds less frequently than moiety 1, but also samples weaker, more distorted interactions (longer H···A distances and more bent angles) on average. This geometric instability provides a mechanistic explanation for the lower interchain cohesion and reduced shearing resistance observed for moiety 6.

References

(1) Li, W. Mechanophores in polymer mechanochemistry: Insights from single-molecule experiments and computer simulations. In *Functional Tactile Sensors*, 2021; pp 113-139.
(2) Ribas-Arino, J.; Shiga, M.; Marx, D. Understanding covalent mechanochemistry. *Angew. Chem., Int. Ed. Engl.* **2009**, *48* (23), 4190-4193.
(3) Rahnamoun, A.; van Duin, A. C. Reactive molecular dynamics simulation on the disintegration of Kapton, POSS polyimide, amorphous silica, and teflon during atomic oxygen impact using the ReaxFF reactive force-field method. *J Phys Chem A* **2014**, *118* (15), 2780-2787.
(4) Duin, A. C. T. v.; Dasgupta, S.; Lorant, F.; III, W. A. G. ReaxFF: A Reactive Force Field for Hydrocarbons. *J. Phys. Chem. A* **2001**, *105*, 9396-9409.
(5) Duin, A. C. T. v.; Strachan, A.; Stewman, S.; Zhang, Q.; Xu, X.; Goddard, W. A. ReaxFFSiO Reactive Force Field for Silicon and Silicon Oxide Systems. *J. Phys. Chem. A* **2003**, *107* (19), 3803-3811.
(6) Neese, F. Software update: The ORCA program system—Version 5.0. *WIREs Computational Molecular Science* **2022**, *12* (5).
(7) Lee, C.; Yang, W.; Parr, R. G. Development of the Colle-Salvetti correlation-energy formula into a functional of the electron density. *Phys Rev B Condens Matter* **1988**, *37* (2), 785-789.
(8) Tirado-Rives, J.; Jorgensen, W. L. Performance of B3LYP density functional methods for a large set of organic molecules. *Journal of Chemical Theory and Computation* **2008**, *4*, 297-306.
(9) Grimme, S.; Antony, J.; Ehrlich, S.; Krieg, H. A consistent and accurate ab initio parametrization of density functional dispersion correction (DFT-D) for the 94 elements H-Pu. *J Chem Phys* **2010**, *132* (15), 154104.
(10) Ahmad, F.; Alam, M. J.; Alam, M.; Azaz, S.; Parveen, M.; Park, S.; Ahmad, S. Synthesis, spectroscopic, computational (DFT/B3LYP), AChE inhibition and antioxidant studies of imidazole derivative. *Journal of Molecular Structure* **2018**, *1151*, 327-342.
(11) Bettens, T.; Eeckhoudt, J.; Hoffmann, M.; Alonso, M.; Geerlings, P.; Dreuw, A.; De Proft, F. Designing Force Probes Based on Reversible 6pi-Electrocyclizations in Polyenes Using Quantum Chemical Calculations. *J Org Chem* **2021**, *86* (11), 7477-7489.
(12) Ribas-Arino, J.; Marx, D. Covalent mechanochemistry: theoretical concepts and computational tools with applications to molecular nanomechanics. *Chem Rev* **2012**, *112* (10), 5412-5487.
(13) Heyes, D. M. Pressure tensor of partial-charge and point-dipole lattices with bulk and surface geometries. *Phys. Rev. B Condens. Matter* **1994**, *49* (2), 755-764.
(14) Thompson, A. P.; Aktulga, H. M.; Berger, R.; Bolintineanu, D. S.; Brown, W. M.; Crozier, P. S.; in 't Veld, P. J.; Kohlmeyer, A.; Moore, S. G.; Nguyen, T. D.; et al. LAMMPS - a flexible simulation tool for particle-based materials modeling at the atomic, meso, and continuum scales. *Comput. Phys. Commun.* **2022**, *271*.
(15) Dodda, L. S.; Vilseck, J. Z.; Tirado-Rives, J.; Jorgensen, W. L. 1.14*CM1A-LBCC: Localized Bond-Charge Corrected CM1A Charges for Condensed-Phase Simulations. *J. Phys. Chem. B* **2017**, *121* (15), 3864-3870.
(16) Dodda, L. S.; Cabeza de Vaca, I.; Tirado-Rives, J.; Jorgensen, W. L. LigParGen web server: an automatic OPLS-AA parameter generator for organic ligands. *Nucleic Acids Res.* **2017**, *45* (W1), W331-W336.
(17) Jorgensen, W. L.; Tirado-Rives. Potential energy functions for atomic-level simulations of water and organic and biomolecular systems. *J. Proc. Nat. Acad. Sci.* **2005**, *102*, 6665-6670.
(18) Arunan, E.; Desiraju, G. R.; Klein, R. A.; Sadlej, J.; Scheiner, S.; Alkorta, I.; Clary, D. C.; Crabtree, R. H.; Dannenberg, J. J.; Hobza, P.; et al. Definition of the hydrogen bond (IUPAC Recommendations 2011). *Pure and Applied Chemistry* **2011**, *83* (8), 1637-1641.
(19) Zheng, K.; Tian, Y.; Fan, M.; Zhang, J.; Cheng, J. Recyclable, shape-memory, and self-healing soy oil-based polyurethane crosslinked by a thermoreversible Diels-Alder reaction. *Journal of Applied Polymer Science* **2018**, *135* (13).
(20) Yang, L.; Du, M.; Yang, S.; Wei, W.; Chang, G. Recyclable Crosslinked High-Performance Polymers via Adjusting Intermolecular Cation-pi Interactions and the Visual Detection of Tensile Strength and Glass Transition Temperature. *Macromol Rapid Commun* **2018**, *39* (10), e1800031.
(21) Wang, C.; Yang, L.; Chang, G. Recyclable Cu(II)-Coordination Crosslinked Poly(benzimidazolyl pyridine)s as High-Performance Polymers. *Macromolecular Rapid Communications* **2018**, *39* (6).

(22) John R. Rumble, e. *CRC Handbook of Chemistry and Physics*; CRC Press/Taylor & Francis, 2023.
(23) Feixas, F.; Matito, E.; Poater, J.; Sola, M. Understanding conjugation and hyperconjugation from electronic delocalization measures. *J Phys Chem A* **2011**, *115* (45), 13104-13113.
(24) Azami, S. M. Electron Density Analysis of Hyperconjugation. *Chemphyschem* **2015**, *16* (18), 3842-3845.
(25) John R. Rumble, e. *CRC Handbook of Chemistry and Physics*; CRC Press/Taylor & Francis, 2023.
(26) Glockler, G. Carbon-Carbon and Carbon-Hydrogen Bond Energies. *J. Chem. Phys.* **1948**, *16* (8), 842-844.
(27) Luo, Y.-R. *Handbook of Bond Dissociation Energies in Organic Compounds*; CRC Press LLC, 2002.
(28) Grinberg, N.; Grushka, E. *Advances in Chromatography*; CRC Press LLC, 2017.
(29) Laurence, C.; Berthelot, M. Observations on the strength of hydrogen bonding. *Perspectives in Drug Discovery and Design* **2000**, *18*, 39-60.
(30) Grinberg, N.; Grushka, E. *Advances in Chromatography*; CRC Press, 2017.